



Electrically driven optical isolation through phonon-mediated photonic Autler-Townes splitting

Donggyu B. Sohn^{1,2}, Oğulcan E. Örsel^{1,2} and Gaurav Bahl^{1,2}

Optical isolators today are exclusively built on magneto-optic principles but are not readily implemented within photonic integrated circuits. So far, no magnetless alternative¹⁻²² has managed to simultaneously combine linearity (that is, no frequency shift), linear response (that is, input-output scaling), ultralow insertion loss and large directional contrast on-chip. Here we demonstrate an electrically driven optical isolator design that leverages the unbeatable transparency of a short, high-quality dielectric waveguide, with the strong attenuation from a critically coupled absorber. Our concept is implemented using a lithium niobate racetrack resonator in which phonon-mediated13 photonic Autler-Townes splitting^{10,16,23,24} breaks the chiral symmetry of the resonant modes. We demonstrate isolators at wavelengths one octave apart near 1,550 nm and 780 nm, fabricated from the same lithium-niobate-on-insulator wafer. Linear isolation is demonstrated with simultaneously <1dB insertion loss, >39 dB contrast and 10 dB bandwidth up to ~200 MHz.

Optical isolators are indispensable in nearly all photonic systems as they help ensure unidirectionality and provide protection from undesirable reflections. Magneto-optic (MO) isolators, based on asymmetric Faraday rotation, have long dominated non-reciprocal photonic device technologies as they simultaneously provide low insertion loss (<2 dB), high directional contrast (30-60 dB) and wide bandwidth (several nanometres). While a number of attempts have been made to bring these devices on chip²⁵⁻³¹, with some measure of success, there remain many unresolved challenges that have held back full adoption. The foremost among these is the lack of appropriate materials in photonics foundries, and the additional technical constraint of magnetic biasing. Recent results^{28,30,31} on integrated MO isolators have been successful at achieving low insertion loss over modest bandwidth; however, they cannot be easily adapted to any wavelength of choice since the Faraday effect is chromatic, that is, it is a strong function of wavelength. Moreover, the MO material stack is intrinsically lossy, and therefore, the best current examples 28,30,31 attempt to use the minimum possible amount of MO material.

Due to a wide recognition of these limitations, extensive research has been performed on alternative isolator and circulator technologies that leverage synthetic fields^{5,6,12,21}, optomechanics^{2,7-11}, acousto-optics^{1,13,14,17-19,22}, electro-optics^{3,4,16,20}, spinning resonators²² and chirally pumped atoms³³. These techniques may be generally considered as variations of spatiotemporal modulation and use some momentum conservation rule or momentum bias to break reciprocity. Often, these approaches operate over a narrow bandwidth, which

is quite acceptable for a wide variety of single-frequency laser applications, for instance, in ultrastable sources^{34,35}, light detection and ranging³⁶, frequency combs³⁷ and atomic referencing³⁸⁻⁴⁰. A number of these alternative techniques have demonstrated very large optical contrast²⁰ (Supplementary Section 7); ultimately, however, the ability to provide low insertion loss remains a huge technical challenge.

The absolute ideal for a two-port low-loss device on chip is simply a high-quality linear waveguide of short length. This represents the best case for achieving the lowest forward insertion loss in the 'high-transparency' direction of an isolator. We now introduce a narrow-band absorber, for example, a high quality factor (high-Q) resonator that is shunt-coupled to this ideal waveguide^{10,15}. If this absorber is detuned more than a few linewidths from the frequency of interest, it will not be accessible to the light propagating within the waveguide and a high transparency is observed (Fig. 1a). On the other hand, when the light is resonant with the absorber and if the absorber is critically coupled to the waveguide (Fig. 1b), a giant attenuation factor can be achieved. Here critical coupling occurs when the intrinsic loss rate for the whispering-gallery resonator (WGR) mode is matched to the coupling rate from the external interface (Supplementary Section 2). It is this combination of near-ideal transparency and giant attenuation that we wish to simultaneously exploit^{10,16}, and it can be achieved using a narrow-band absorber with broken chiral symmetry (Fig. 1c).

In this Letter, we report a method to induce very large chiral asymmetry in a two-level photonic atom using phonon-mediated photonic Autler-Townes splitting (p-ATS)^{10,13,16}. Here p-ATS is the splitting of non-degenerate optical modes caused by an externally driven field, in analogy to ATS in electronic systems^{30,41}. When coupled with a waveguide, the resulting isolator exhibits near-ideal characteristics. The two-level photonic atom is produced using a WGR that supports two families of optical modes belonging to the transverse electric TE₁₀ and TE₀₀ families. We identify a mode pair that is closely spaced in frequency near a mode-family crossing, with the TE₀₀ mode (ω_1, k_1) and TE₁₀ mode (ω_2, k_2) having distinct frequencies (ω) and wavevectors (k), as shown in Fig. 1d. These two modes can be unidirectionally coupled through acousto-optic scattering, as long as the difference in frequency $(\Omega = \omega_2 - \omega_1)$ and momentum $(q = k_2 - k_1)$ between the optical modes matches the frequency Ω and momentum q of an acoustic excitation of the material. In addition, the overlap integral between the acoustic mode and optical modes must be non-zero¹³. Both these requirements, while tricky, can be simultaneously achieved by the engineering of a two-dimensional (2D) 'texture' for the acoustic excitation of the resonator^{13,17}, such that there is a non-zero momentum along the WGR LETTERS NATURE PHOTONICS

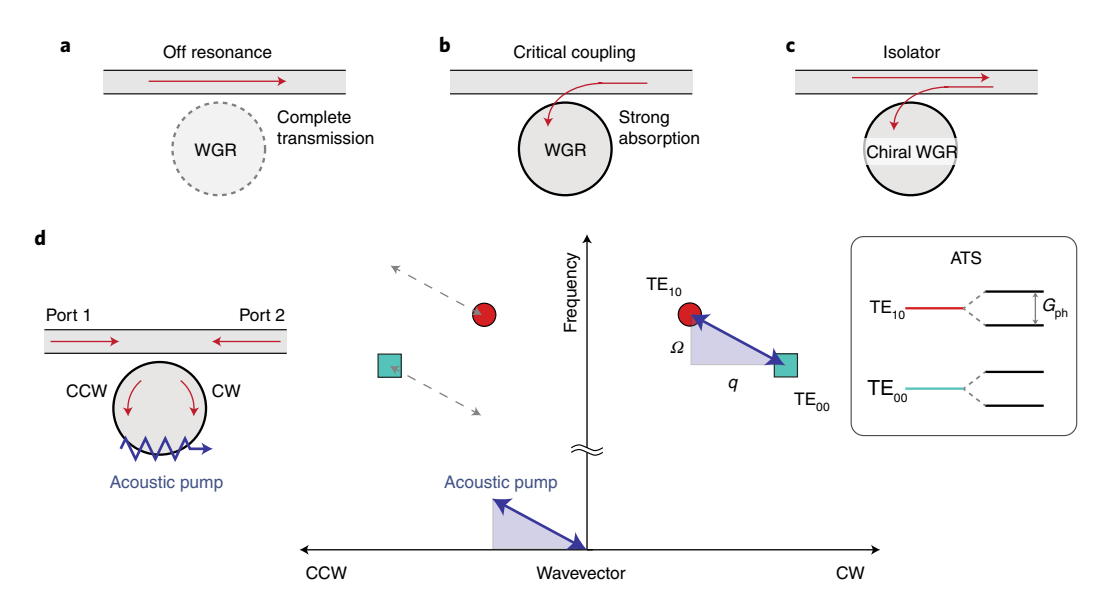


Fig. 1 | Optical isolation with a chiral absorber. a, For a waveguide-resonator system, any light that propagates detuned far from the resonance of the absorber (here a WGR) passes through the waveguide uninterrupted. Propagation loss is primarily dictated by the waveguide quality. b, If the waveguide and WGR are critically coupled, a nearly complete on-resonance absorption situation is achieved. **c**, For a photonic WGR with chiral density of states, there exist frequencies where—depending on the propagation direction in the waveguide—complete transparency and strong attenuation can be simultaneously achieved. **d**, We use phonon-mediated ATS in a two-level photonic atom (the TE_{10} and TE_{00} modes of the WGR act as the coupled levels) to produce the chiral WGR. In the diagram, the ATS appears only for optical wavevectors corresponding to clockwise circulation due to the acousto-optic phase-matching condition. The phonon-enhanced optomechanical coupling rate G_{ph} determines the amount of level splitting that is generated. CW, clockwise; CCW, counterclockwise.

circuit, while a standing wave exists in the transverse direction. When the phonon-enhanced optomechanical coupling rate (G_{ph}) exceeds the optical loss rates $(G_{ph} > \sqrt{\kappa_1 \kappa_2})$, we enter the strong coupling or p-ATS regime (Supplementary Section 1). This regime manifests as unidirectional hybridization of the selected TE₁₀ and TE₀₀ modes, modifying their dispersion and splitting the frequency of resonant absorption in the phase-matched direction only. In this analogy, $G_{\rm ph}$ determines the amount of frequency splitting and is equivalent to the Rabi frequency in atomic ATS. In this situation, light propagating at the original optical resonance frequencies (ω_1 and ω_2) in the waveguide no longer interacts with the resonator and simply propagates through it. This will be the case as long as the process is reasonably well phase matched, and the coupling rate $G_{\rm ph}$ is sufficiently large. In the non-phase-matched direction, however, the original optical modes remain unmodified. Thus, the fundamental limit to the isolator bandwidth is set by the original optical modes. If we additionally design the system to achieve critical coupling for the TE₁₀ mode, then giant contrast is simultaneously achieved (Supplementary Section 2). As a result of this architecture, our approach achieves unidirectional strong coupling and large non-reciprocity with a single radio-frequency (RF) input, without requiring multiple phase-shifted signals, which is common in other spatiotemporal modulation approaches.

For experimental implementation, we used a lithium-niobate-on-insulator-integrated photonics platform. The wide bandgap of lithium niobate (LN) imparts a broad transparency window spanning from 350 to 5,300 nm. Additionally, the high piezoelectric coefficient of LN allows very efficient actuation of surface acoustic waves via RF stimulus⁴², which is a specific advantage for this device. In contrast to previous efforts that used aluminium nitride as the photonic and piezoelectric material 13,17 , here we are able to achieve much higher optical Q-factors (10^7 at 780 nm and 3.5×10^6 at 1,550 nm) and substantially better electromechanical transduction efficiency (about ten times higher at 40%). The two-mode race-

track resonators and adjacent single-mode waveguides (Fig. 2a) are etched with ridge waveguide geometry (Supplementary Section 5). Grating couplers covering the wavelength range of interest are fabricated on either end of the waveguide to provide off-chip optical access to the isolator. Finally, to ensure the transverse standing-wave characteristic for acoustic excitation, we fabricate an acoustic reflector by fully etching the LN thin film on the far side of the racetrack (Fig. 2a,b).

We first characterize the primary acoustic and optical components of the isolator. Measurement of the RF reflection coefficient (RF S₁₁) of the interdigitated (IDT) actuator shows a dip near 3 GHz, confirming the excitation of the surface acoustic wave (Fig. 2c). The optical states of the racetrack resonator are measured by probing the transmission through the adjacent waveguide. As shown in Fig. 2d, two optical-mode families can be identified, where the TE₁₀ family is better coupled to the waveguide due to its larger evanescent field. In fact, the TE₁₀ mode is critically coupled to the waveguide to ensure maximum attenuation in the backward direction. The TE_{00} mode is kept intentionally dark (that is, undercoupled) since it is helpful to both lower the G_{ph} requirement and to suppress sideband generation (as discussed later). The device is designed such that there is a mode crossing near the wavelength of interest. For the specific device shown, we find an optical-mode pair located near 192.6 THz (1,556 nm) that has a frequency separation of ~3.0 GHz, which is similar to the acoustic frequency. Finally, a constant RF tone at 3 GHz is applied to the IDT actuator, which launches the 2D surface acoustic wave and hybridizes the two optical modes, producing the p-ATS.

We experimentally measure the non-reciprocal transmission using optical heterodyne detection (Supplementary Section 6), which enables a separate measurement of the carrier signal transmission and its sidebands. Figure 2e shows the evolution of the optical spectrum for increasing RF driving power, in both phase-matched (optical S_{21}) and non-phase-matched (optical S_{12}) directions through

NATURE PHOTONICS LETTERS

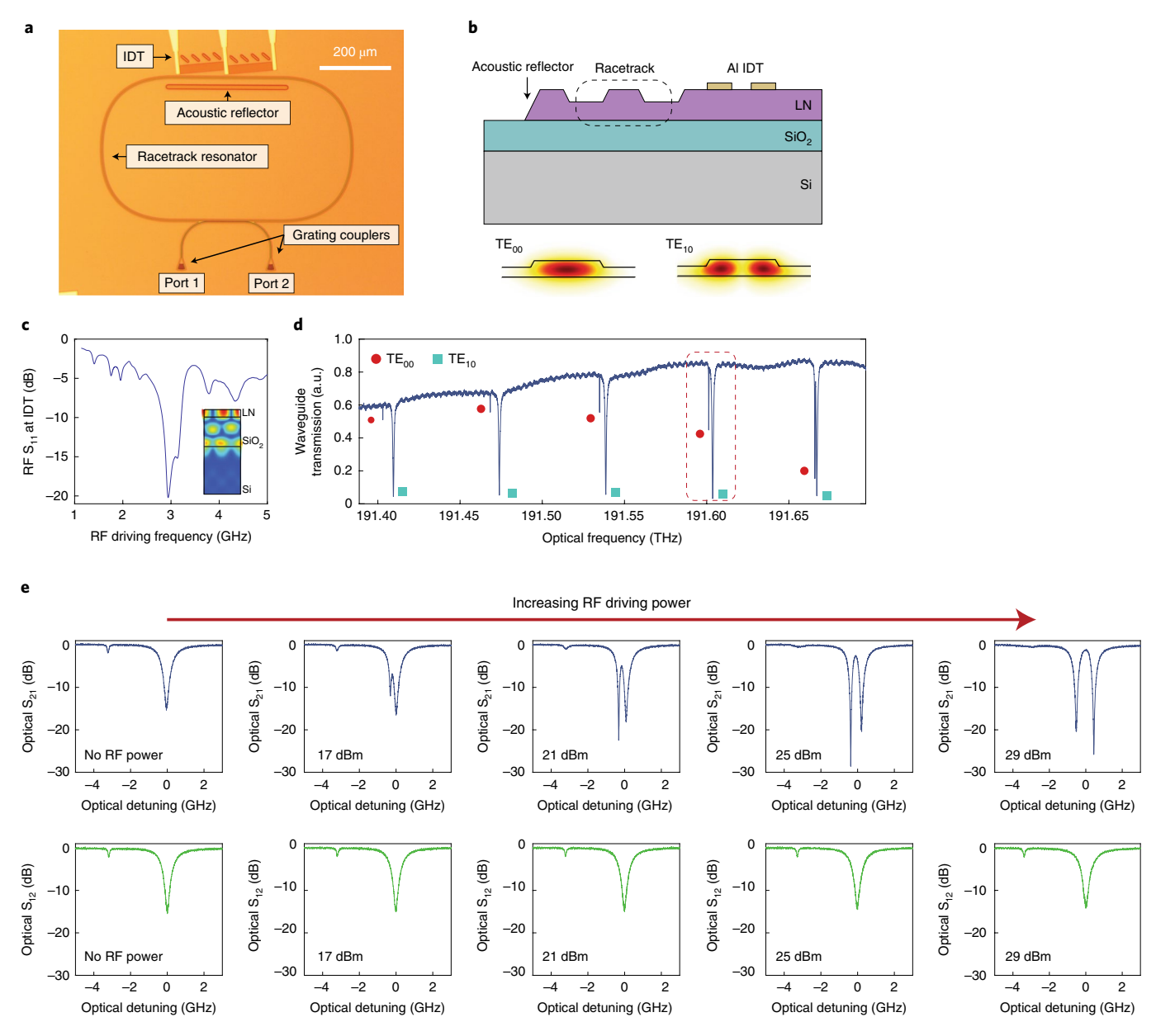


Fig. 2 | Implementation and characterization of phonon-mediated p-ATS isolator. **a**, Microscopy image of the LN optical isolator. The device is composed of a racetrack WGR with an adjacent waveguide. The required 2D surface acoustic wave 'texture' is produced using an angled IDT actuator and acoustic reflector on opposite sides of the racetrack. **b**, Cross-section of the acousto-optic interaction region shows the racetrack resonator (modes are presented in the inset) with an aluminium IDT actuator and acoustic reflector. The device is unreleased. **c**, IDT actuator characterization using RF reflection measurement (RF S_{11} parameter) shows that the surface acoustic wave in this device is efficiently generated at around 3 GHz, as determined by the designed IDT actuator pitch and surface acoustic wave speed. Inset: a cross-section simulation of the surface acoustic mode, with redder colours corresponding to regions of higher mechanical strain. **d**, Optical characterization (transmission through the waveguide) without any applied RF stimulus. **e**, As the RF power applied to the IDT actuator increases, the optical S_{21} (transmission from port 1 to port 2) and S_{12} (transmission from port 2 to port 1) measurements performed through the waveguide exhibit phonon-mediated p-ATS in only one direction. A closer examination of this isolator is presented in Fig. 3a.

the waveguide ports. We factor out the grating coupler losses in optical S-parameter measurements (Supplementary Section 6) as these devices are intended to be monolithically integrated into larger photonic circuits. The frequency of the original TE_{10} mode is defined as the zero-detuning (Δ =0) point. In the phase-matched direction, the optical modes experience a clear p-ATS phenomenon, with the central transmission at zero detuning approaching unity for large drive power. At the same time, the optical modes remain unperturbed in the non-phase-matched direction.

A closer examination of the telecommunication-wavelength (1,550 nm) isolator is presented in Fig. 3a. We observe that this

device simultaneously achieves a forward insertion loss of 1.13 dB with peak contrast of 12.75 dB using 29 dBm of RF driving power. This drive level corresponds to a phonon-enhanced optomechanical coupling rate $G_{\rm ph}$ of 0.98 GHz, and we are currently prevented from increasing this further due to the power-handling capability of the IDT actuators. The non-reciprocal contrast here is limited only by the degree to which we are able to approach the critical coupling in the fabricated device. While our main attention is on the central isolation behaviour, we also observe appreciable non-reciprocity on the wings corresponding to the dressed states, although absorption occurs in the opposite (phase-matched) direction in this case.

LETTERS NATURE PHOTONICS

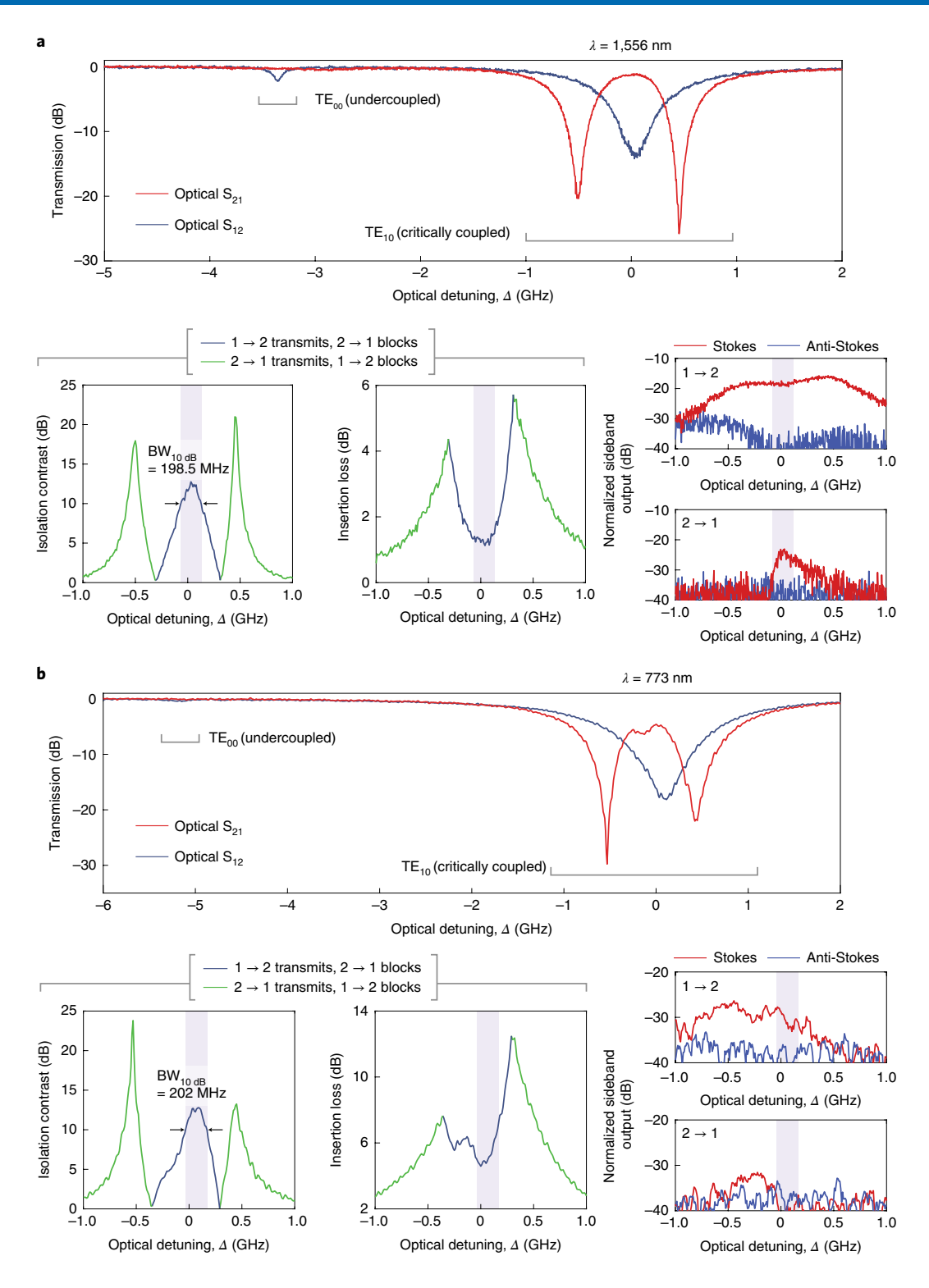


Fig. 3 | Experimental demonstration of phonon-mediated p-ATS isolators near 1,550 and 780 nm. Detuning Δ is defined relative to the unperturbed TE₁₀ mode. **a**, Measurement results from a 1,556 nm device for 3.00 GHz applied RF with 29 dBm power (measured $G_{ph} \approx 0.98$ GHz). **b**, Measurement results from a 773 nm device for 5.05 GHz applied RF with 25 dBm power (measured $G_{ph} \approx 0.99$ GHz). BW, bandwidth. A discussion is provided in the main text and additional details on the device parameters can be found in Supplementary Table 2.

During the experiment, we are also able to monitor the $\pm 3\,\mathrm{GHz}$ sidebands of the carrier signal, and we find that they are consistently ~20 dB below (or above) the original carrier signal power. This is owing to a combination of the very high G_{ph} , which significantly reduces the interaction between the waveguide and WGR at

 Δ = 0, as well as the undercoupled TE $_{00}$ mode that does not couple well to the waveguide. Further discussion is provided in Supplementary Section 3.

Since all the features of this device are lithographically defined and they do not depend on the gyrotropic property of any NATURE PHOTONICS LETTERS

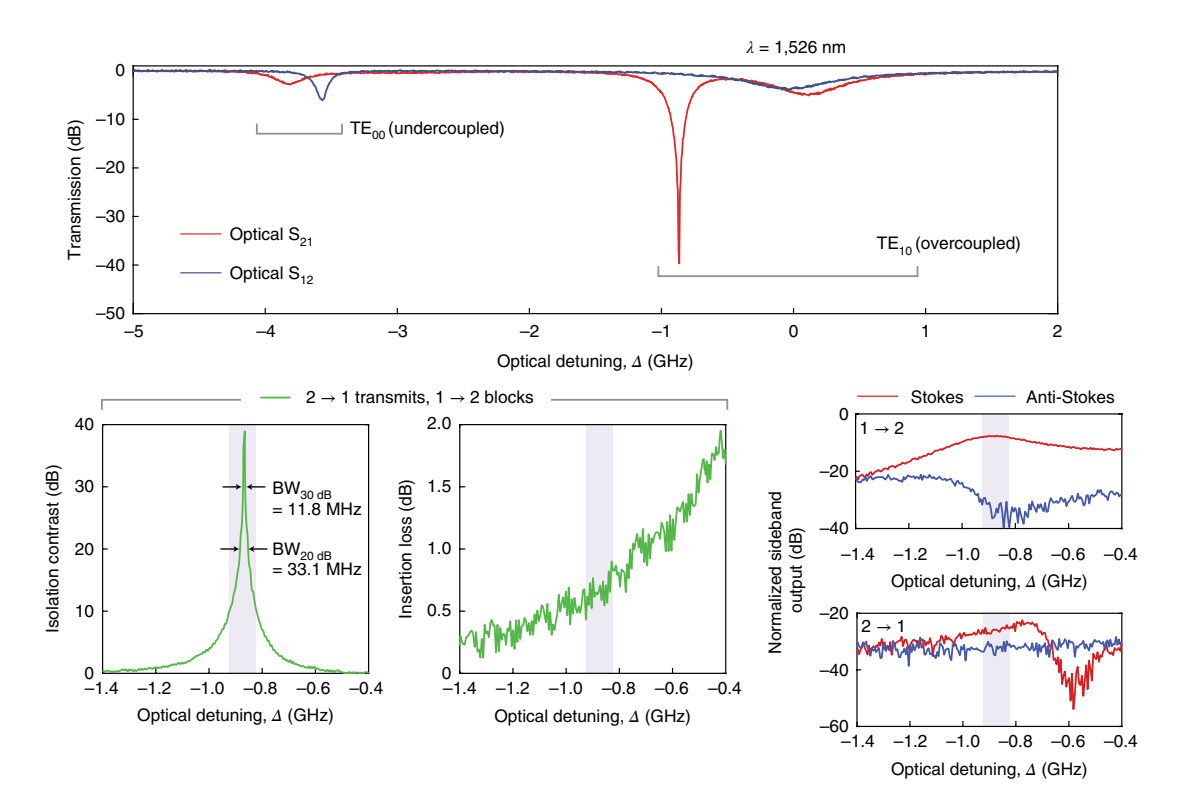


Fig. 4 | Demonstration of giant isolation using dressed state non-reciprocity. Detuning Δ is defined relative to the unperturbed TE₁₀ mode. Measurement results from a 1,526 nm isolator for 3.04 GHz applied RF with 29 dBm power (measured $G_{ph} \approx 0.76$ GHz). Another example of this effect for a device operating near 780 nm is shown in Supplementary Fig. 4. Additional details on the device parameters can be found in Supplementary Table 2.

wavelength-dependent material (for example, the Faraday rotation effect in magneto-optics), we are able to shift the operational wavelength of this isolator freely within the transparency range of LN. In fact, optomechanical coupling $G_{\rm ph}$ is directly proportional to the optical frequency, implying that isolators operating at short wavelengths with comparable parameters will require lower power. There is, however, the possibility that this advantage is offset by the generally higher surface-scattering-induced loss at short wavelengths. In this context, we developed a 780 nm demonstration (Fig. 3b) for the isolator using the same lithium-niobate-on-insulator substrate. This device simultaneously achieves a forward insertion loss of 4.76 dB with peak contrast of 12.86 dB, using 25 dBm of RF driving power to reach $G_{\rm ph} \approx 0.99$ GHz. While the insertion loss achieved in this device was not as low, sideband generation is significantly reduced since the TE00 mode is very undercoupled.

In the above p-ATS-based approach, the isolation contrast is primarily dictated by the criticality of coupling between the waveguide and optical mode (here the TE₁₀ mode) and is therefore strongly dependent on the fabricated geometry. Contrast factors greater than 25 dB can, therefore, be difficult to achieve because of the matching requirement with the intrinsic resonator loss. One solution to the contrast problem is instead leveraging the non-reciprocal wings to either side of the central non-reciprocal band. In these bands, the contrast is dictated by the placement of and coupling to the dressed states. The contrast is, therefore, a function of $G_{\rm ph}$ and of the relative mismatch $\delta = \omega_1 - \omega_2 + \Omega$ between the optical-mode separation and applied phonon frequency. Additional discussion of this situation is provided in Supplementary Section 4. As a key result, we find that if the TE₁₀ mode is intentionally overcoupled and the mode mismatch is δ < 0, then there exists a choice of G_{ph} where critical coupling is achievable near the lower dressed state. Conversely, for $\delta > 0$, critical coupling is achievable near the upper dressed state. A dramatic example of this situation is presented for an overcoupled 1,538 nm

isolator (Fig. 4); on the lower dressed state, we can simultaneously observe 0.65 dB insertion loss with 39.3 dB contrast using 29 dBm of RF driving power to reach $G_{\rm ph}\approx 0.76$ GHz. Here spacing between the optical modes is 3.72 GHz while the RF drive is at 3.04 GHz, implying $\delta\approx -0.68$ GHz. We also implemented this effect with opposite δ using a device operating near 780 nm (Supplementary Fig. 4).

We can understand this phenomenon fairly intuitively by considering instead a sideband picture, which works since the mismatch δ puts the system in a regime between pure ATS and the alternating current Stark effect (the latter explains the noticeable frequency shifts in the modes). As we scan the overcoupled TE₁₀ mode (that is, intrinsic loss rate less than extrinsic coupling rate), we find a range of frequencies where the scattering into the undercoupled TE₀₀ mode is resonantly enhanced. This implies that as $G_{\rm ph}$ increases, the effective intrinsic loss rate of the TE₁₀ mode over this band increases, and can approach the extrinsic coupling rate to hit criticality. This intuitive explanation is also experimentally supported by the increased Stokes sideband power in the $2\rightarrow 1$ case (Fig. 4), which indicates increased scattering into the TE₀₀ mode. While this approach is much more sensitive to the value of G_{ph} , unlike the central isolation band, the tunability of this operating regime can be advantageous and ultimately delivers better results in the devices shown in this paper.

Since isolators are often used in cascaded configurations, citing insertion loss (IL) or isolation contrast (IC) alone is not meaningful. Instead, as discussed previously¹⁰, the ratio of IC per dB of IL is the relevant figure of merit that accounts for cascading. We find that this device (Fig. 4) not only provides IC at par with the best MO isolators, but significantly outperforms them on IL and isolator figure of merit (comparison shown in Supplementary Section 7). The main disadvantage of our approach compared with magneto-optics is the narrower operational bandwidth, which is another equally important figure of merit for isolators. In our approach, the isolation

LETTERS NATURE PHOTONICS

bandwidth is fundamentally limited by the optical-mode shape and—to an extent—can be increased by lowering the optical Q-factor while increasing $G_{\rm ph}$ to achieve the same insertion loss. Ultimately, terahertz-range isolation may be reachable by extending our approach to non-resonant systems^{4,22}, although extremely large $G_{\rm ph}$ will be necessary to achieve competitive insertion loss. A solution to significantly increase the bandwidth thus remains an open challenge. In the interim, the addition of electro-optic or thermo-optic frequency tunability would be a clear path towards increasing the utility of the isolators demonstrated in this work.

The lack of optical isolators in photonic integrated circuits has long been a technological hurdle, and their absence is uniquely felt by contemporary quantum and atomic microsystems. Isolator and circulator banks are extensively used in low-temperature quantum technologies to suppress thermal noise, but stray magnetic fields from available isolators can be problematic for superconducting materials, for example, in qubits. Magnetless isolators working in the visible and near-infrared wavelengths are also critically needed to enable chip-scale atom-photon integration^{38,39,43}, as they can circumvent undesirable Zeeman shifts⁴⁴. The isolators demonstrated by us are extremely well positioned to address these applications, as they exhibit narrow-band performance at par with current off-chip MO isolators, while simultaneously providing access to wavelength ranges that are challenging with MO techniques.

Note added in proof: We recently became aware of a related optical isolator implementation by Tian et al. 45.

Online content

Any methods, additional references, Nature Research reporting summaries, source data, extended data, supplementary information, acknowledgements, peer review information; details of author contributions and competing interests; and statements of data and code availability are available at https://doi.org/10.1038/s41566-021-00884-x.

Received: 8 April 2021; Accepted: 21 August 2021; Published online: 21 October 2021

References

- Hwang, I. K., Yun, S. H. & Kim, B. Y. All-fiber-optic nonreciprocal modulator. Opt. Lett. 22, 507–509 (1997).
- Kang, M. S., Butsch, A. & Russell, P. S. J. Reconfigurable light-driven opto-acoustic isolators in photonic crystal fibre. *Nat. Photon.* 5, 549–553 (2011).
- 3. Doerr, C. R., Dupuis, N. & Zhang, L. Optical isolator using two tandem phase modulators. *Opt. Lett.* **36**, 4293–4295 (2011).
- Lira, H., Yu, Z., Fan, S. & Lipson, M. Electrically driven nonreciprocity induced by interband photonic transition on a silicon chip. *Phys. Rev. Lett.* 109, 033901 (2012).
- Tzuang, L. D., Fang, K., Nussenzveig, P., Fan, S. & Lipson, M. Non-reciprocal phase shift induced by an effective magnetic flux for light. *Nat. Photon.* 8, 701–705 (2014).
- Li, E., Eggleton, B. J., Fang, K. & Fan, S. Photonic Aharonov–Bohm effect in photon–phonon interactions. *Nat. Commun.* 5, 3225 (2014).
- Sounas, D. L. & Alù, A. Angular-momentum-biased nanorings to realize magnetic-free integrated optical isolation. ACS Photon. 1, 198–204 (2014).
- Dong, C.-H. et al. Brillouin-scattering-induced transparency and non-reciprocal light storage. *Nat. Commun.* 6, 6193 (2015).
- Kim, J., Kuzyk, M. C., Han, K., Wang, H. & Bahl, G. Non-reciprocal Brillouin scattering induced transparency. *Nat. Phys.* 11, 275–280 (2015).
- Kim, J., Kim, S. & Bahl, G. Complete linear optical isolation at the microscale with ultralow loss. Sci. Rep. 7, 1647 (2017).
- Ruesink, F., Miri, M.-A., Alù, A. & Verhagen, E. Nonreciprocity and magnetic-free isolation based on optomechanical interactions. *Nat. Commun.* 7, 13662 (2016).
- Fang, K. et al. Generalized non-reciprocity in an optomechanical circuit via synthetic magnetism and reservoir engineering. *Nat. Phys.* 13, 465–471 (2017).
- Sohn, D. B., Kim, S. & Bahl, G. Time-reversal symmetry breaking with acoustic pumping of nanophotonic circuits. *Nat. Photon.* 12, 91–97 (2018).

- Kittlaus, E. A., Otterstrom, N. T., Kharel, P., Gertler, S. & Rakich, P. T. Non-reciprocal interband Brillouin modulation. *Nat. Photon.* 12, 613–619 (2018).
- Peterson, C. W., Kim, S., Bernhard, J. T. & Bahl, G. Synthetic phonons enable nonreciprocal coupling to arbitrary resonator networks. Sci. Adv. 4, eaat0232 (2018).
- Shi, Y., Lin, Q., Minkov, M. & Fan, S. Nonreciprocal optical dissipation based on direction-dependent Rabi splitting. *IEEE J. Sel. Topics Quantum Electron*. 24, 1–7 (2018).
- Sohn, D. B. & Bahl, G. Direction reconfigurable nonreciprocal acousto-optic modulator on chip. APL Photon. 4, 126103 (2019).
- Tian, H. et al. Hybrid integrated photonics using bulk acoustic resonators. Nat. Commun. 11, 3073 (2020).
- Sarabalis, C. J. et al. Acousto-optic modulation of a wavelength-scale waveguide. Optica 8, 477–483 (2021).
- Dostart, N., Gevorgyan, H., Onural, D. & Popović, M. Optical isolation using microring modulators. Opt. Lett. 46, 460–463 (2021).
- Kim, S., Sohn, D. B., Peterson, C. W. & Bahl, G. On-chip optical non-reciprocity through a synthetic Hall effect for photons. APL Photon. 6, 011301 (2021).
- Kittlaus, E. A. et al. Electrically driven acousto-optics and broadband non-reciprocity in silicon photonics. *Nat. Photon.* 15, 43–52 (2021).
- Peng, B., Özdemir, Ş. K., Chen, W., Nori, F. & Yang, L. What is and what is not electromagnetically induced transparency in whispering-gallery microcavities. *Nat. Commun.* 5, 5082 (2014).
- Zhang, M. et al. Electronically programmable photonic molecule. *Nat. Photon.* 13, 36–40 (2019).
- Bi, L. et al. On-chip optical isolation in monolithically integrated non-reciprocal optical resonators. Nat. Photon. 5, 758–762 (2011).
- Ghosh, S. et al. Ce:YIG/silicon-on-insulator waveguide optical isolator realized by adhesive bonding. Opt. Express 20, 1839–1848 (2012).
- Huang, D. et al. Dynamically reconfigurable integrated optical circulators. Optica 4, 23–30 (2017).
- Zhang, C., Dulal, P., Stadler, B. J. H. & Hutchings, D. C. Monolithically-integrated TE-mode 1D silicon-on-insulator isolators using seedlayer-free garnet. Sci. Rep. 7, 5820 (2017).
- Du, Q. et al. Monolithic on-chip magneto-optical isolator with 3 dB insertion loss and 40 db isolation ratio. ACS Photon. 5, 5010–5016 (2018).
- Zhang, Y. et al. Monolithic integration of broadband optical isolators for polarization-diverse silicon photonics. Optica 6, 473–478 (2019).
- Yan, W. et al. Waveguide-integrated high-performance magneto-optical isolators and circulators on silicon nitride platforms. Optica 7, 1555–1562 (2020).
- 32. Maayani, S. et al. Flying couplers above spinning resonators generate irreversible refraction. *Nature* **558**, 569–572 (2018).
- Scheucher, M., Hilico, A., Will, E., Volz, J. & Rauschenbeutel, A. Quantum optical circulator controlled by a single chirally coupled atom. *Science* 354, 1577–1580 (2016).
- 34. Spencer, D. T. et al. An optical-frequency synthesizer using integrated photonics. *Nature* **557**, 81–85 (2018).
- Lucas, E. et al. Ultralow-noise photonic microwave synthesis using a soliton microcomb-based transfer oscillator. *Nat. Commun.* 11, 374 (2020).
- Poulton, C. V. et al. Coherent solid-state LIDAR with silicon photonic optical phased arrays. Opt. Lett. 42, 4091–4094 (2017).
- Del'Haye, P. et al. Optical frequency comb generation from a monolithic microresonator. *Nature* 450, 1214–1217 (2007).
- 38. Hummon, M. T. et al. Photonic chip for laser stabilization to an atomic vapor with 10^{-11} instability. *Optica* 5, 443–449 (2018).
- Knappe, S. et al. A microfabricated atomic clock. Appl. Phys. Lett. 85, 1460–1462 (2004).
- Newman, Z. L. et al. Architecture for the photonic integration of an optical atomic clock. Optica 6, 680–685 (2019).
- Peng, B. et al. Parity-time-symmetric whispering-gallery microcavities. Nat. Phys 10, 394–398 (2014).
- Gong, S. & Piazza, G. Design and analysis of lithium–niobate-based high electromechanical coupling RF-MEMS resonators for wideband filtering. *IEEE Trans. Microw. Theory Techn.* 61, 403–414 (2013).
- Riedel, M. F. et al. Atom-chip-based generation of entanglement for quantum metrology. Nature 464, 1170–1173 (2010).
- Blanshan, E., Rochester, S. M., Donley, E. A. & Kitching, J. Light shifts in a pulsed cold-atom coherent-population-trapping clock. *Phys. Rev. A* 91, 041401 (2015).
- 45. Tian, H. et al. Magnetic-free silicon nitride integrated optical isolator. Preprint at https://arxiv.org/abs/2104.01158 (2021).

Publisher's note Springer Nature remains neutral with regard to jurisdictional claims in published maps and institutional affiliations.

© The Author(s) 2021

NATURE PHOTONICS LETTERS

Data availability

The data that support the findings of this study are available from the corresponding author upon reasonable request.

Code availability

All relevant code is available from the corresponding author upon reasonable request.

Acknowledgements

This work was sponsored by the Defense Advanced Research Projects Agency (DARPA) grant FA8650-19-2-7924, the National Science Foundation EFRI grant EFMA-1641084 and the Air Force Office of Scientific Research (AFOSR) grant FA9550-19-1-0256. G.B. additionally acknowledges support from the Office of Naval Research (ONR) Director for Research Early Career grant N00014-17-1-2209 and the Presidential Early Career Award for Scientists and Engineers. D.B.S. acknowledges support from a US National Science Foundation Graduate Research Fellowship. We also thank K. Chow at the Holonyak Micro & Nanotechnology Lab (HMNTL) at the University of Illinois for valuable advice and guidance. The US Government is authorized to reproduce and distribute reprints for Governmental purposes notwithstanding any copyright notation thereon. The views and conclusions contained herein are those of the authors and should not be interpreted as necessarily representing

the official policies or endorsements, either expressed or implied, of DARPA or the US Government.

Author contributions

D.B.S., O.E.Ö. and G.B. jointly conceived the isolator concept. D.B.S. and O.E.Ö. performed the device fabrication, conducted the experimental measurements and analysed the data. All the authors contributed to writing the paper. G.B. supervised all aspects of this project.

Competing interests

The authors declare no competing interests.

Additional information

Supplementary information The online version contains supplementary material available at https://doi.org/10.1038/s41566-021-00884-x.

Correspondence and requests for materials should be addressed to Gaurav Bahl.

Peer review information *Nature Photonics* thanks Chun-Hua Dong and the other, anonymous, reviewer(s) for their contribution to the peer review of this work.

Reprints and permissions information is available at www.nature.com/reprints.